

Analysis and Comparison of Peak-to-Peak Current Ripple in Two-Level and Multilevel PWM Inverters

Gabriele Grandi, *Senior Member, IEEE*, Jelena Loncarski, *Student Member, IEEE*, and Obrad Dordevic, *Member, IEEE*

Abstract—Three-phase multilevel (ML) inverters are used in many medium- and high-power applications such as motor drives and grid-connected systems. Despite the fact that numerous pulsewidth modulation (PWM) techniques for ML inverters have been developed, the impact of these modulation schemes on the peak-to-peak output current ripple amplitude has not been addressed yet. In this paper, analysis and comparison of current ripple for two-level (2L) and three-level (3L) voltage source inverters are given. Reference is made to optimal and popular modulation, so-called centered PWM, easily obtained by both carrier-based modulation (phase disposition, with proper common-mode voltage injection) and space vector modulation (nearest three vectors). It is shown that the peak-to-peak current ripple amplitude in 3L inverters can be determined on the basis of the ripple in 2L inverters, obtaining the same results as by directly analyzing the output voltage waveforms of the 3L inverters. This procedure can be readily extended to higher level numbers. The proposed analytical developments are verified by both numerical simulations and experimental tests.

Index Terms—Carrier-based pulsewidth modulation (PWM), multilevel (ML) inverters, output current ripple, space vector (SV) PWM, three-level (3L) inverter.

I. INTRODUCTION

THREE-PHASE two-level (2L) inverters are widely utilized in ac motor drives and, in general, for grid-connected applications. In the last decades, multilevel (ML) inverters have become more and more popular, due to improved output voltage waveforms and increased power ratings. In particular, the ML structure is capable of reaching high output voltage amplitudes by using standard power switches with limited voltage ratings.

Simple and reliable implementations of ML inverters are the cascaded connection of single-phase inverters (H-bridge) and the neutral point clamped (NPC) configuration. Among ML inverters, the three-level (3L) inverters are a viable solution for

many high-power applications, both grid connected and motor load.

Since the performance of an inverter mainly depends on its modulation strategy, many PWM techniques have been developed in the last decades for 2L and ML inverters [1]–[13]. Generally, these modulation techniques can be classified into two categories: carrier-based (CB) and space-vector (SV) modulation. It has been proved that phase disposition (PD) CB modulation and nearest three vectors (NTV) SV modulation for 2L and ML inverters can be equivalent [4], [9]–[12]. In particular, PD CB-PWM leads to the same output voltages as the SV-PWM if a proper common-mode voltage is injected into the modulating signals. On the other hand, CB-PWM can be equivalently realized by NTV SV-PWM through a proper sharing of dwell times among the redundant switching states. Specifically, the nearly optimal modulation so-called centered PWM (CPWM) is obtained by sharing dwell times among the redundant switching states, offering reduced harmonic distortion in output currents [4], [9]–[13].

The impact and comparison of CPWM schemes on the peak-to-peak output current ripple amplitude in 2L and ML inverters has not been addressed yet. In [14], the current ripple trajectory in α – β coordinates for the case of dual-inverter-fed open-end winding load configuration, operating as a 3L inverter, is shown. However, emphasis was made on current ripple root mean square (RMS) rather than on the instantaneous ripple. The evaluation of peak-to-peak current ripple for 2L three-phase PWM inverters was first briefly introduced in [15] and better developed in [16]. A similar procedure has been proposed in [17], with further developments and insights but without experimental verifications. The same analysis has been extended to multiphase inverters in [18]–[21].

In general, for both 2L and ML inverters, the peak-to-peak current ripple distribution is useful in determining multiple zero-crossing intervals of the output current and the corresponding dead-time output voltage distortion [22]. Furthermore, knowledge of current ripple amplitude can be used to compare PWM and hysteresis current controllers [23]–[25] and to define variable switching frequency PWM techniques [26].

This paper gives the evaluation and the comparison of the output current ripple amplitude in 2L and ML inverters. It is shown that the peak-to-peak current ripple amplitude in 3L and ML inverters can be obtained on the basis of the ripple evaluation in 2L inverters (which has been already addressed in the literature), by introducing the known concept of pivot voltage vector in the 3L and ML case instead of null voltage vector in

Manuscript received April 12, 2014; revised April 21, 2014 and July 17, 2014; accepted September 20, 2014. Date of publication October 17, 2014; date of current version April 8, 2015.

G. Grandi is with the Department of Electrical, Electronic, and Information Engineering, University of Bologna, 40136 Bologna, Italy (e-mail: gabriele.grandi@unibo.it).

J. Loncarski is with the Department of Engineering Sciences, Ångström Laboratory, Uppsala University, 751 21 Uppsala, Sweden (e-mail: jelena.loncarski@angstrom.uu.se).

O. Dordevic is with the School of Engineering, Liverpool John Moores University, Liverpool, L3 3AF, U.K. (e-mail: O.Dordevic@ljmu.ac.uk).

Color versions of one or more of the figures in this paper are available online at <http://ieeexplore.ieee.org>.

Digital Object Identifier 10.1109/TIE.2014.2363624

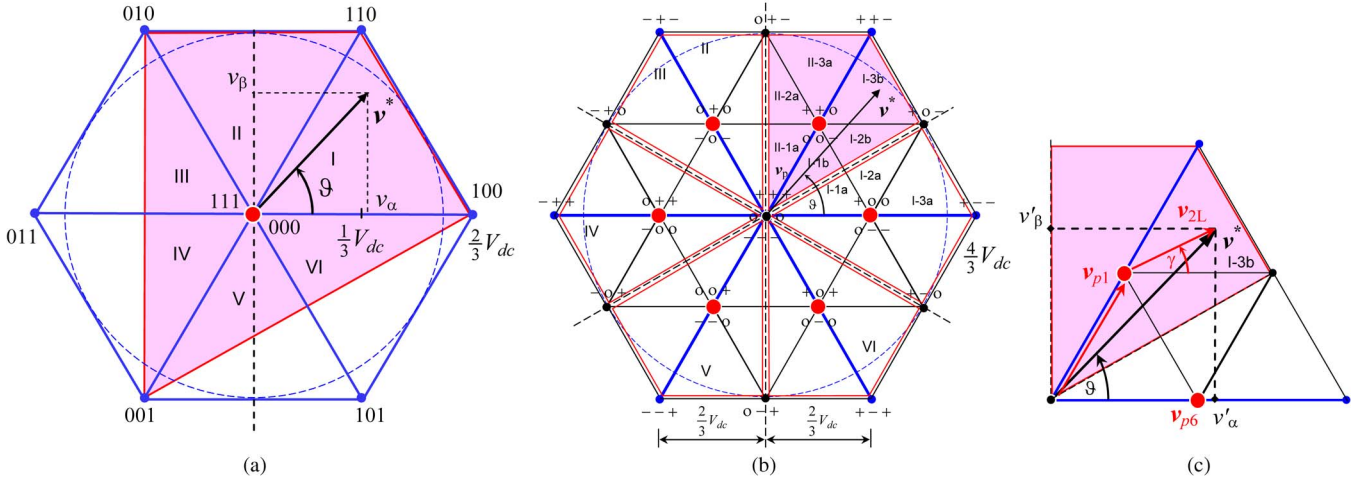


Fig. 1. SV diagrams of inverter output voltage. (a) 2L inverter. (b) 3L inverter. (c) Details of one of the six main triangles and subtriangle (I-3b).

the 2L case [27]. It is also shown that the results obtained with this method are the same compared with the results obtained directly by analyzing the output voltage waveforms of the 3L inverter. The peak-to-peak ripple amplitude is introduced as a function of the modulation index over a fundamental period, considering centered PWM switching patterns obtained either by CB- or SV-PWM techniques [11]–[13]. The instantaneous current ripple is determined for a generic balanced three-phase load consisting of series RL impedance and ac back-electromotive force (RLE-load), representing both motor-load and grid-connected applications. The ripple analysis is verified by both numerical simulations and experimental tests in the case of both 2L and 3L inverters, for different modulation indexes in the linear modulation range.

II. SPACE VECTOR ANALYSIS AND PWM EQUATIONS

The use of SVs in the analysis of 2L and ML three-phase inverters is introduced here since it leads to better understanding and more simple calculation of voltage levels and corresponding application times. The switching states of the k th inverter phase can be denoted as $S_k = [0, 1]$ for the 2L inverter and as $S_k = [-1, 0, 1]$, i.e., $\{-0+\}$, for the 3L inverter. Further coefficients can be introduced for higher level numbers [7], [8]. In this way, the output voltage vector v of 2L and ML inverters can be expressed by

$$v = \frac{2}{3} V_{dc} [S_1 + S_2 \alpha + S_3 \alpha^2] \quad (1)$$

V_{dc} being the dc supply voltage and $\alpha = \exp(j2\pi/3)$.

Fig. 1 shows the output voltage SVs corresponding to all possible switch configurations in 2L and 3L inverters [see Fig. 1(a) and (b)]. For both inverters, the SV diagram appears to be a hexagon divided into six main triangles, i.e., sectors I–VI. Note that by supplying each ML cell of the 3L inverter with the same dc voltage of the 2L inverter, the resulting hexagon size is doubled, corresponding to double output voltage capability for the 3L inverter.

In addition to the redundant states corresponding to the null vector, there are six further redundant states corresponding to vertices of the inner hexagon, called pivot (or base) states in the

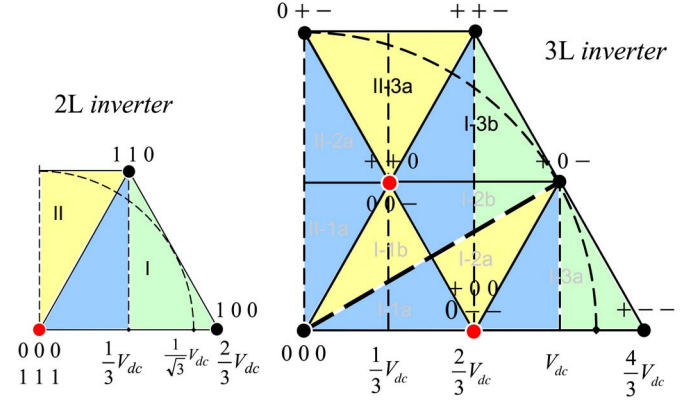


Fig. 2. 2L and 3L inverter voltage diagrams in the first quadrant of the α – β plane.

3L inverter [27]. The SV-PWM scheme uses the NTV algorithm to approximate the reference output voltage vector. In the case of continuous modulation strategies, the switching sequence starts from one pivot state, goes to the other switching states, and comes back to the first. Beginning and ending states of this traverse correspond to the same pivot (base) vector, that is the null vector in the case of 2L inverters, and one of the six small vectors (magnitude $2/3 V_{dc}$) in the case of 3L inverters (v_p , enlarged red dots in Fig. 1). This modulation principle can be extended to any ML inverter by a proper identification of NTV [7], [8].

The working domain of each pivot vector is the subhexagon centered on it. In the case of the 3L inverter, it is restricted to a diamond-shaped region (pivot sector, pink colored area in Fig. 1 for v_{p1}), due to the overlaps between subhexagons.

For sinusoidal balanced output voltages, the reference output voltage vector is $v^* = V^* \exp(j\vartheta)$, being $V^* = m V_{dc}$, $\vartheta = \omega t$. Note that the limits of modulation index m are $0 \leq m \leq 1/\sqrt{3}$ for the 2L inverter and $0 \leq m \leq 2/\sqrt{3}$ for the 3L inverter. The analysis can be restricted to the first quadrant in the considered case of quarter-wave symmetric SV modulation.

The SV modulation of 3L and ML inverters can be traced back to the one of 2L inverter by considering the reference voltage v^* as the combination of pivot voltage v_p and residual 2L reference voltage v_{2L} , for each pivot sector [see Fig. 1(c)].

TABLE I
SWITCH CONFIGURATION DUTY CYCLES FOR 2L AND 3L INVERTERS

2L inverter			
	δ_1	δ_2	δ_0
I	$\frac{3}{2}(u_\alpha - 1/\sqrt{3}u_\beta)$	$\sqrt{3}u_\beta$	$1 - \frac{3}{2}(u_\alpha + 1/\sqrt{3}u_\beta)$
II	$\frac{3}{2}(u_\alpha + 1/\sqrt{3}u_\beta)$	$\frac{3}{2}(1/\sqrt{3}u_\beta - u_\alpha)$	$1 - \sqrt{3}u_\beta$
3L inverter			
	δ_1	δ_2	δ_p
I-3b	$\frac{3}{2}(u'_\alpha - 1/\sqrt{3}u'_\beta)$	$\sqrt{3}u'_\beta - 1$	$2 - \frac{3}{2}(u'_\alpha + 1/\sqrt{3}u'_\beta)$
II-3a	$\frac{3}{2}(u'_\alpha + 1/\sqrt{3}u'_\beta) - 1$	$\frac{3}{2}(1/\sqrt{3}u'_\beta - u'_\alpha)$	$2 - \sqrt{3}u'_\beta$

Application times t_k of NTV are defined by duty cycles δ_1 , δ_2 , and δ_0 , i.e., δ_p , for 2L, i.e., 3L inverters, and switching period T_s , being $\delta_k = t_k/(T_s/2)$. The duty cycles for the first quadrant of the 2L inverter and the corresponding quadrant of pivot vector v_{p1} for the 3L inverter (see Fig. 2) are given in Table I. Normalized reference voltages u_α and u_β used in Table I are defined as

$$\begin{cases} u_\alpha = \frac{v_\alpha}{V_{dc}} = m \cos \vartheta, & u_\beta = \frac{v_\beta}{V_{dc}} = m \sin \vartheta & \text{for 2L} \\ u'_\alpha = \frac{v'_\alpha}{V_{dc}} = m \cos \vartheta, & u'_\beta = \frac{v'_\beta}{V_{dc}} = m \sin \vartheta & \text{for 3L} \end{cases} \quad (2)$$

α and β being the indexes for real and imaginary components of v^* , as represented in Fig. 1(a) and (c). The calculation of the duty cycles could be easily extended to the other sectors for 2L, 3L, and ML inverters [2], [7], [8].

In centered SV-PWM of 2L and ML inverters, the application time of the pivot vector (δ_0 or δ_p) is shared in equal parts for the two redundant pivot states. In this way, a nearly optimal modulation, able to minimize the RMS of current ripple, is obtained [4], [11]. Considering CB-PWM, an equivalent switching pattern can be achieved by injecting a proper common-mode signal to the reference voltage waveforms. In this way, the resulting modulating signals are able to equally share the application times of redundant states. While for 2L inverters a simple min/max injection can be used for centering [2], a more complex common-mode signal has to be added to reference voltages in case of ML inverters [9]–[12]. A simplified procedure to obtain the centered optimized modulating signals has been recently introduced in [13] for the 3L case.

In this paper, the ripple analysis is developed for centered SV modulation, implemented by carrier-based PWM, being one of the most popular 2L and ML modulations. In particular, CB-PWM offers inherent simplicity, flexibility, reduced computational time, and easy implementation on industrial digital signal processors, without the need for field-programmable gate array or any other additional hardware.

III. PEAK-TO-PEAK CURRENT RIPPLE EVALUATION

Due to the symmetry among the three phases in the considered case of sinusoidal balanced currents, only the first phase is examined in the following analysis. The current ripple defini-

tion introduced in [17] is recalled here for better understanding. The basic equation for an RLE circuit, representing both motor-load and grid-connected systems, is

$$v(t) = Ri(t) + L \frac{di}{dt} + v_g(t). \quad (3)$$

Averaging (3) and introducing the current variation $\Delta i = i(T_s) - i(0)$ in the switching period T_s gives

$$\bar{v}(T_s) = R\bar{i}(T_s) + L \frac{\Delta i}{T_s} + \bar{v}_g(T_s). \quad (4)$$

The alternating voltage $\tilde{v}(t)$ is defined as the difference between instantaneous and average voltage components as

$$\tilde{v}(t) = v(t) - \bar{v}(T_s). \quad (5)$$

The instantaneous current ripple can be calculated by substituting (3) and (4) in (5) and integrating

$$\tilde{i}(t) = \Delta i(t) - \frac{t}{T_s} \Delta i \cong \frac{1}{L} \int_0^t \tilde{v}(t) dt. \quad (6)$$

This procedure is discussed with more details in [17]–[19]. Note that the current ripple calculated by (6) corresponds to the difference between the instantaneous current and its fundamental component.

The peak-to-peak current ripple amplitude is defined as the range of (6) in the switching period

$$\tilde{i}_{pp} = \max \left\{ \tilde{i}(t) \right\}_0^{T_s} - \min \left\{ \tilde{i}(t) \right\}_0^{T_s}. \quad (7)$$

In terms of SVs, the variables of the first phase are given by the projection of the corresponding SVs on the real axis. In particular, if the reference voltage is within the modulation limits, i.e., the reference SV v^* lies within the outer hexagon, the average output voltage is given by

$$\bar{v}(T_s) = v^* = \text{Re}\{v^*\} = V^* \cos \vartheta = V_{dc} m \cos \vartheta. \quad (8)$$

The instantaneous output voltage of the first phase can be expressed by switching states defined in (1), leading to

$$v(t) = V_{dc} \left[S_1 - \frac{1}{3}(S_1 + S_2 + S_3) \right]. \quad (9)$$

The alternating voltage component for 2L and ML inverters can be determined by introducing (8) and (9) in (5), i.e.,

$$\tilde{v}(t) = V_{dc} \left[S_1 - \frac{1}{3}(S_1 + S_2 + S_3) \right] - m V_{dc} \cos \vartheta. \quad (10)$$

In order to evaluate the current ripple for both 2L and 3L inverters, only the three cases identified by the three different colored areas in Fig. 2 can be separately considered. The results are readily extended to the whole hexagons by exploiting the quarter-wave symmetry.

The analytical developments for ML inverters can be carried out by considering the residual reference voltage v_{2L} instead of the original reference voltage v^* , for each pivot vector v_p , as emphasized by the pink-colored regions in Fig. 1.

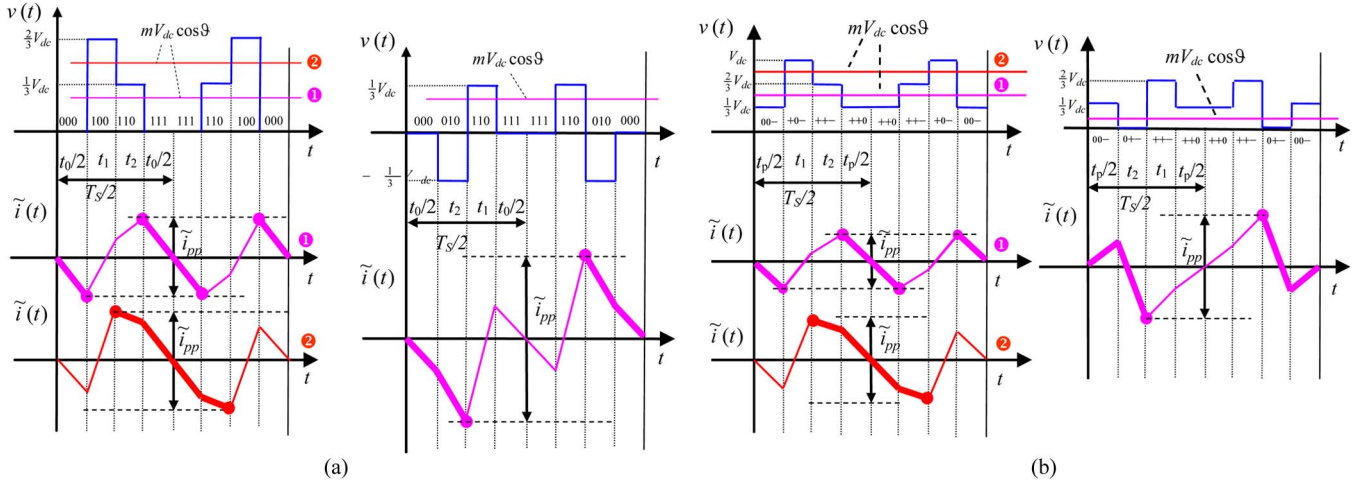


Fig. 3. Output voltage and current ripple in one switching period (a) for the 2L inverter (sectors I and II) and (b) for the 3L inverter (triangles I-3b and II-3a).

A. Evaluation for the 2L Inverter

The ripple evaluation in the case of the 2L inverter is summarized here since it is the basis of the proposed analysis for ML inverters. Considering the 2L inverter, two different cases can be distinguished in sector I: $0 \leq m \cos \vartheta \leq 1/3$ and $m \cos \vartheta \geq 1/3$, and one single case for half the sector II, corresponding to the three colored areas in Fig. 2.

The subcase $0 \leq m \cos \vartheta \leq 1/3$, corresponding to the blue area of sector I in Fig. 2, is shown in diagram ① in Fig. 3(a). In particular, the current ripple and its peak-to-peak value are depicted, together with the instantaneous output voltage $v(t)$. In this case, \tilde{i}_{pp} can be evaluated by (6), (7), and (10), considering either switch configuration {111} or {000}, and the corresponding application time $t_0/2$, i.e., duty cycle $\delta_0/2$, according to Fig. 3(a). Normalizing by (2) gives

$$\tilde{i}_{pp} = \frac{V_{dc}T_s}{2L} \{m \cos \vartheta \delta_0\} = \frac{V_{dc}T_s}{2L} \{u_\alpha \delta_0\}. \quad (11)$$

Peak-to-peak current ripple can also be expressed as

$$\tilde{i}_{pp} = \frac{V_{dc}T_s}{2L} r(m, \vartheta) \quad (12)$$

$r(m, \vartheta)$ being the normalized peak-to-peak current ripple amplitude. Introducing in (11) the expression of δ_0 given in Table I, the normalized current ripple becomes

$$r(m, \vartheta) = u_\alpha \left[1 - \frac{3}{2} \left(u_\alpha + \frac{1}{\sqrt{3}} u_\beta \right) \right]. \quad (13)$$

The subcase $1/3 \leq m \cos \vartheta \leq 1/\sqrt{3}$, corresponding to the green area of sector I in Fig. 2, is depicted in diagram ② in Fig. 3(a). In this case, \tilde{i}_{pp} can be evaluated considering both the switch configurations {111} and {110} with the corresponding duty cycles $\delta_0/2$ and δ_2 . Normalizing by (2) gives

$$\tilde{i}_{pp} = \frac{V_{dc}T_s}{2L} \left\{ u_\alpha \delta_0 + 2 \left(u_\alpha - \frac{1}{3} \right) \delta_2 \right\}. \quad (14)$$

Introducing in (14) the expression of δ_0 and δ_2 given in Table I, the normalized current ripple becomes

$$r(m, \vartheta) = u_\alpha \left[1 - \frac{3}{2} \left(u_\alpha + \frac{1}{\sqrt{3}} u_\beta \right) \right] + 2\sqrt{3}u_\beta \left(u_\alpha - \frac{1}{3} \right). \quad (15)$$

The only subcase of the half of sector II, corresponding to the yellow area in Fig. 2, is depicted in Fig. 3(a) (right-hand side). In this case, \tilde{i}_{pp} can be evaluated considering both the switch configurations {000} and {010} with the corresponding duty cycles $\delta_0/2$ and δ_2 . Normalizing by (2) gives

$$\tilde{i}_{pp} = \frac{V_{dc}T_s}{2L} \left\{ u_\alpha \delta_0 + 2 \left(u_\alpha + \frac{1}{3} \right) \delta_2 \right\}. \quad (16)$$

Substituting in (16) the expression of δ_0 and δ_2 given in Table I for sector II, the normalized current ripple becomes

$$r(m, \vartheta) = u_\alpha [1 - \sqrt{3}u_\beta] + 3 \left(\frac{1}{\sqrt{3}}u_\beta - u_\alpha \right) \left(u_\alpha + \frac{1}{3} \right). \quad (17)$$

The analysis can be easily extended to all the other sectors of the 2L hexagon by exploiting the quarter-wave symmetry.

B. Evaluation for the 3L Inverter

Two different ways to analyze the current ripple in the 3L inverter are presented in this subsection. The first is based on the results of the 2L case introduced in the previous section, resulting in a simpler and more general analysis. The alternative method is based on the direct analysis of 3L voltage waveforms, leading to more involved calculations, and used here just to verify the results in the considered cases.

The ripple analysis in the case of more than two levels can be carried out by taking into account that in each pivot sector the role of the pivot vector is similar to the role of the null vector in the 2L inverter, according to the pink areas emphasized in Fig. 1 in case of the 3L inverter. Considering the vector composition represented in Fig. 1(c), the normalized reference voltages of the 3L inverter can be written as

$$u'_\alpha = u_\alpha + 1/3, \quad u'_\beta = u_\beta + 1/\sqrt{3} \quad (18)$$

where u_α and u_β are the normalized reference voltages corresponding to the 2L inverter. From (18), the expressions of the 2L reference voltages can be derived as

$$u_\alpha = u'_\alpha - 1/3, \quad u_\beta = u'_\beta - 1/\sqrt{3}. \quad (19)$$

The subcase $m \cos \vartheta \leq 2/3$, related to the blue area of triangle I-3b in Fig. 2, corresponds to the blue area of sector I in the 2L inverter. \tilde{i}_{pp} can be evaluated introducing (19) in the expression obtained for 2L inverter (11), leading to

$$\tilde{i}_{pp} = \frac{V_{dc}T_s}{2L} \left\{ \left[u'_\alpha - \frac{1}{3} \right] \delta_0 \right\} \quad (20)$$

where δ_0 can be obtained by introducing (19) in the expression of the duty cycle of the 2L inverter given in Table I. The normalized current ripple for the 3L inverter becomes

$$\begin{aligned} r(m, \vartheta) &= \left(u'_\alpha - \frac{1}{3} \right) \left[1 - \frac{3}{2} \left(\left(u'_\alpha - \frac{1}{3} \right) + \frac{1}{\sqrt{3}} \left(u'_\beta - \frac{1}{\sqrt{3}} \right) \right) \right] \\ &= \left(u'_\alpha - \frac{1}{3} \right) \left[2 - \frac{3}{2} \left(u'_\alpha + \frac{1}{\sqrt{3}} u'_\beta \right) \right]. \end{aligned} \quad (21)$$

An alternative method to derive the peak-to-peak ripple amplitude for the 3L inverter is to analyze the output voltage waveforms, as done for the 2L inverter. The considered subcase corresponding to the blue area of triangle I-3b in Fig. 2 is depicted in diagram ① in Fig. 3(b). In this case, \tilde{i}_{pp} can be evaluated by (6), (7), and (10), considering the switch configuration $\{+ + 0\}$ or $\{0 0 -\}$, according to Fig. 3(b), with the corresponding duty cycle $\delta_p/2$, leading to

$$\tilde{i}_{pp} = \frac{V_{dc}T_s}{2L} \left\{ \left(m \cos \vartheta - \frac{1}{3} \right) \delta_p \right\} = \frac{V_{dc}T_s}{2L} \left\{ \left(u'_\alpha - \frac{1}{3} \right) \delta_p \right\}. \quad (22)$$

After introducing the expression for δ_p given in Table I for the 3L inverter and normalization, the current ripple becomes

$$r(m, \vartheta) = \left(u'_\alpha - \frac{1}{3} \right) \left[2 - \frac{3}{2} \left(u'_\alpha + \frac{1}{\sqrt{3}} u'_\beta \right) \right]. \quad (23)$$

Comparing (23) with expression (21) obtained with the analysis based on the 2L inverter, the matching is verified.

The subcase $m \cos \vartheta > 2/3$, related to the green area of triangle I-3b in Fig. 2, corresponds to the green area of sector I in the 2L inverter. Starting from the expression derived for the 2L inverter (14) and introducing (19), the peak-to-peak current ripple can be written as

$$\tilde{i}_{pp} = \frac{V_{dc}T_s}{2L} \left\{ \left(u'_\alpha - \frac{1}{3} \right) \delta_0 + 2 \left[\left(u'_\alpha - \frac{1}{3} \right) - \frac{1}{3} \right] \delta_2 \right\} \quad (24)$$

where δ_0 and δ_2 are the duty cycles of the 3L inverter obtained by substituting (19) in the expressions of duty cycles of the 2L inverter given in Table I. The normalized current ripple for the 3L inverter becomes

$$\begin{aligned} r(m, \vartheta) &= \left(u'_\alpha - \frac{1}{3} \right) \left[2 - \frac{3}{2} \left(u'_\alpha + \frac{1}{\sqrt{3}} u'_\beta \right) \right] \\ &\quad + 2 \left(u'_\alpha - \frac{2}{3} \right) (\sqrt{3} u'_\beta - 1). \end{aligned} \quad (25)$$

As in the previous case, peak-to-peak ripple amplitude can also be obtained by directly analyzing the output voltage waveforms. The considered subcase, representing the green area of triangle I-3b in Fig. 2, is depicted in diagram ② in Fig. 3(b). In this case, \tilde{i}_{pp} can be evaluated considering the switch configurations $\{+ + 0\}$ and $\{+ + -\}$ and the corresponding duty cycles $\delta_p/2$ and δ_2 , leading to

$$\tilde{i}_{pp} = \frac{V_{dc}T_s}{2L} \left\{ \left(m \cos \vartheta - \frac{1}{3} \right) \delta_p + 2 \left(m \cos \vartheta - \frac{2}{3} \right) \delta_2 \right\}. \quad (26)$$

After introducing the expressions for δ_p and δ_2 given in Table I for the 3L inverter and normalization, current ripple becomes

$$\begin{aligned} r(m, \vartheta) &= \left(u'_\alpha - \frac{1}{3} \right) \left[2 - \frac{3}{2} \left(u'_\alpha + \frac{1}{\sqrt{3}} u'_\beta \right) \right] \\ &\quad + 2 \left(u'_\alpha - \frac{2}{3} \right) (\sqrt{3} u'_\beta - 1). \end{aligned} \quad (27)$$

Comparing (27) with expression (25) obtained with the analysis based on the 2L inverter, the matching is verified.

The subcase related to the yellow area of the half triangle II-3a in Fig. 2 corresponds to the yellow area of the half of sector II in the 2L inverter. In this case, \tilde{i}_{pp} can be evaluated by substituting (19) in the expression obtained for 2L inverter (16), leading to

$$\tilde{i}_{pp} = \frac{V_{dc}T_s}{2L} \left\{ \left(u'_\alpha - \frac{1}{3} \right) \delta_0 + 2 \left[\left(u'_\alpha - \frac{1}{3} \right) + \frac{1}{3} \right] \delta_2 \right\} \quad (28)$$

where δ_0 and δ_2 can be obtained by introducing (19) in the expressions of duty cycles of the 2L inverter given in Table I. The normalized current ripple for the 3L inverter becomes

$$r(m, \vartheta) = \left(u'_\alpha - \frac{1}{3} \right) (2 - \sqrt{3} u'_\beta) + 3 u'_\alpha \left(\frac{1}{\sqrt{3}} u'_\beta - u'_\alpha \right). \quad (29)$$

As in the previous cases, peak-to-peak ripple amplitude can also be obtained by directly analyzing the output voltage waveforms. The considered subcase is depicted Fig. 3(b) (right-hand side). In this case, \tilde{i}_{pp} can be evaluated considering the switch configurations $\{+ + 0\}$ and $\{0 + -\}$ and the corresponding duty cycles $\delta_p/2$ and δ_2 , leading to

$$\tilde{i}_{pp} = \frac{V_{dc}T_s}{2L} \left\{ \left(m \cos \vartheta - \frac{1}{3} \right) \delta_p + 2 m \cos \vartheta \delta_2 \right\}. \quad (30)$$

After introducing the expressions of δ_p and δ_2 given in Table I for the 3L inverter and normalization, current ripple becomes

$$r(m, \vartheta) = \left(u'_\alpha - \frac{1}{3} \right) (2 - \sqrt{3} u'_\beta) + 3 u'_\alpha \left(\frac{1}{\sqrt{3}} u'_\beta - u'_\alpha \right). \quad (31)$$

Comparing (31) with expression (29) obtained with the analysis based on the 2L inverter, the matching is verified.

The analysis can be easily extended to the entire considered pivot sector and to all the other pivot sectors of the 3L inverter

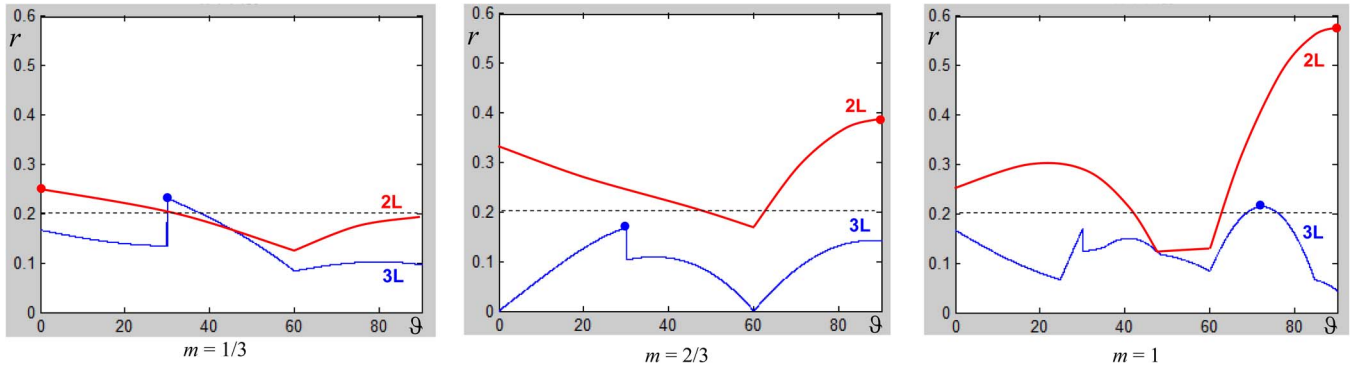


Fig. 4. Normalized peak-to-peak current ripple amplitude $r(m, \vartheta)$ for 2L and 3L inverters in the range $\vartheta = [0, 90^\circ]$ for different modulation indexes.

by exploiting the quarter-wave symmetry (corresponding colored areas in Fig. 2). Moreover, by exploiting the algorithm proposed here, i.e., the calculation of the ripple for 3L inverters on the basis of the ripple in 2L inverters, the analysis can be easily extended to the general case of ML inverters. This is in contrast to the extension of the direct method, which is leading to more involved calculations.

C. Ripple Comparison Between 2L and 3L Inverters

In order to show and compare the behavior of the peak-to-peak current ripple amplitude in the fundamental period, the same output voltage range for 2L and 3L inverters should be considered. For this reason, the 2L inverter is supplied by double dc voltage, $2V_{dc}$, i.e., all the derived ripple expressions are multiplied by 2, whereas each cell of the 3L inverter is supplied by V_{dc} . With this assumption, the modulation index is $0 \leq m \leq 2/\sqrt{3}$ for both 2L and 3L inverters.

In Fig. 4, the normalized function $r(m, \vartheta)$ defined by (12) for $m = 1/3$, $2/3$, and 1 , is shown in the case of 2L and 3L inverters. As expected, the ripple in the 3L inverter is lower than the ripple in the 2L inverter almost for the whole phase angle range. In the same figure, the maximum normalized current ripple (r^{\max}) is emphasized with dots. It is noted that r^{\max} has a reduced variability with m , almost close to the value 0.2 (dashed line) in the case of 3L inverter, whereas r^{\max} is increasing almost proportionally with m in the case of 2L inverter [17]. This is due to the lower distance between the reference vector \mathbf{v}^* and the available voltage vectors in the case of 3L inverter, exploited by applying the NTV modulation. The discontinuity noticed in the current ripple envelope of the 3L inverter for $\vartheta = 30^\circ$ is introduced by the pivot vector change, i.e., six times in the fundamental period. This discontinuity is easily recognizable in the modulating signals of centered CB-PWM in the case of 3L inverters [11]–[13], whereas the modulating signals are continuous in the 2L case. Note that there is not discontinuity at $\vartheta = \pm 90^\circ$ for the sake of the symmetry. A better view of this discontinuity from the point of view of SVs is shown in the following colored map of current ripple.

In Fig. 5, the average of normalized current ripple, i.e., r_{avg} , is shown as a function of the modulation index to summarize the current ripple amplitude in the whole fundamental period. Three different cases are considered: 2L inverter supplied by V_{dc} and $2V_{dc}$ and 3L inverter supplied by V_{dc} . It can be

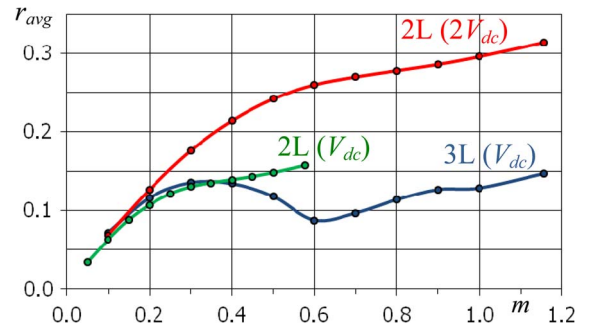


Fig. 5. Average normalized current ripple versus modulation index.

noticed that the 2L inverter supplied with $2V_{dc}$ has almost the double of the average normalized ripple compared with the 3L inverter, except for low modulation indexes, i.e., less than 0.4 . The 2L inverter supplied with V_{dc} shows a lower ripple than the 3L inverter for $m < 1/3$, whereas for $m > 1/3$ up to the modulation limit of the 2L inverter ($1/\sqrt{3}$), the ripple is lower for the 3L inverter. The lower ripple in case of the 2L inverter for low modulation indexes (inner hexagon) can be explained with reference to the considered CB modulation. Namely, for 3L inverters, the centered SV-PWM shares the pivot states into two equal parts and offers reduced harmonic distortion in the output currents. However, it is not the most optimal modulation within the inner hexagon (corresponding to the hexagon in the 2L inverter), since the used pivot vectors are not the zero vector. The centered SV-PWM modulation in the 2L inverter, which uses the zero vector as the pivot vector, is known to be the most optimal in this case.

Fig. 5 also shows that r_{avg} has a reduced excursion in the case of 3L inverter, oscillating between 0.075 and 0.15 for $m = [0.1, 1]$, whereas it is a monotonic increasing function of m ranging in a wider range in the case of 2L inverter. The average current ripple amplitude can be also used to compare the performance of 2L and 3L PWM inverters with current-hysteresis-controlled inverters, having a current ripple amplitude that is almost constant.

Fig. 6 shows the colored maps of $r(m, \vartheta)$ in the first quadrant within the modulation limits for 2L and 3L inverters. The discontinuity of the ripple across the border of pivot sectors (red line) in the 3L inverter is now well observed, due to the pivot vector change. Namely, the red line divides the two pivot sectors (one of pivot vector \mathbf{v}_{p1} and another of \mathbf{v}_{p6}). In the case

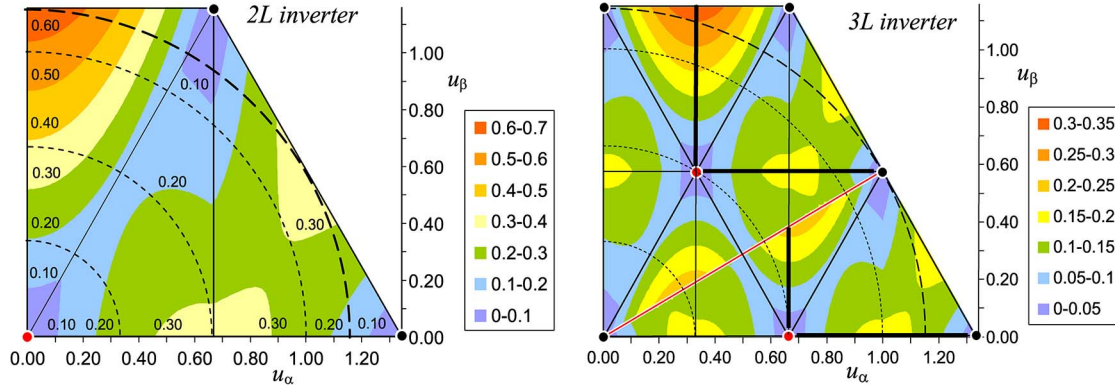


Fig. 6. Maps of the normalized peak-to-peak current ripple amplitude $r(m, \vartheta)$ for the 2L inverter (supplied by $2V_{dc}$) and the 3L inverter (supplied by V_{dc}).

of subtriangles I-1a and I-2a, the pivot vector applied is v_{p6} , whereas in the case of subtriangles I-1b and I-2b, the pivot vector is v_{p1} . Note that the pivot vector determines the sequence of applied voltage levels. As a consequence, also within the same NTV, i.e., the same available voltage levels, a pivot change causes a different current ripple.

For both 2L and 3L inverters, it can be noted that ripple amplitude is going to zero in the surroundings of each output voltage vector, since the reference vector is almost perfectly synthesized and the alternating voltage (5) goes to zero. Although in Fig. 6 the same colors for both ripple maps are kept, the color scale for the 2L inverter is double than for the 3L inverter. The first quadrant ripple map of the 2L inverter is emphasized with bold lines in the ripple map of the 3L inverter, for each pivot vector.

IV. RESULTS

In order to verify the analytical developments proposed in the previous sections, numerical simulations and corresponding experimental tests are carried out. Circuit simulations are performed by Sim-PowerSystems of MATLAB considering both 2L and 3L inverters with ideal switches, i.e., no dead-time was implemented in order to match perfectly the theoretical developments. Experimental tests are carried out by custom-made converters. In particular, the 2L inverter is implemented by Infineon FS50R12KE3 insulated-gate bipolar transistor (IGBT) pack, and the 3L inverter (NPC type) is implemented by Semikron SKM50GB12T4 IGBT modules, with Semikron SKKD 46/12 clamping diodes. The dSpace ds1006 hardware has been employed for the real-time implementation of algorithms. The experimental setups of 2L and 3L inverters are shown in Fig. 7.

In order to compare 2L and 3L inverters with the same output voltage capabilities, 600 V total dc voltage supply ($2V_{dc}$) was provided from Sorensen SGI 600/25 for both inverters. With this assumption, analytical developments are carried out with $V_{dc} = 300$ V and $0 \leq m \leq 2/\sqrt{3}$ for both 2L and 3L inverters.

Switching frequency was set to 2.1 kHz, and a dead-time of $6 \mu s$ (not compensated) was implemented in the hardware. Fundamental frequency was kept at 50 Hz for easier comparison with analytical developments. The nearly optimal centered CB PWM is implemented, leading to equally share the application times of pivot vectors.

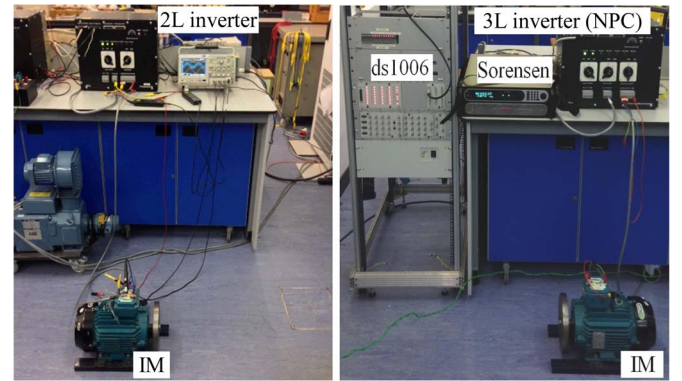


Fig. 7. Experimental setups of 2L and 3L inverters.

For both 2L and 3L inverters, the load was a three-phase induction motor (mechanically unloaded) having the following stator-referred parameters: stator resistance $R_s = 2.4 \Omega$, rotor resistance $R'_r = 1.6 \Omega$, stator leakage inductance $L_{ls} = 12$ mH, rotor leakage inductance $L'_{lr} = 12$ mH, magnetizing inductance $L_m = 300$ mH, two pole pairs. According to the model of induction motor for higher order harmonics, which are determining the current ripple, the estimated total equivalent inductance $L = L_{ls} + L'_{lr} = 24$ mH is considered for the ripple evaluation.

Tektronix oscilloscope MSO2014 with current probe TCP 0030 was used for measurements, and the built-in noise filter (cutoff frequency $f_c = 600$ kHz) was applied. A further low-pass filter ($f_c = 25$ kHz) was applied in post-processing of the experimental data to better clean the waveforms from the switching noise. The instantaneous current ripple is calculated as the difference between instantaneous and fundamental current components, according to (6), i.e.,

$$\tilde{i}(t) = i(t) - i_{fund}(t). \quad (32)$$

As in the previous sections, the first phase is selected for further analysis, and different values of m are investigated to cover the different subcases in the whole linear modulation index range.

Figs. 8–10 show simulation and corresponding experimental results for $m = 1/3$, $2/3$, and 1, respectively. In particular, for all figures, the upper diagrams show the simulation results (pink traces) and the calculated ripple envelopes (blue traces). The bottom diagrams show the corresponding experimental results

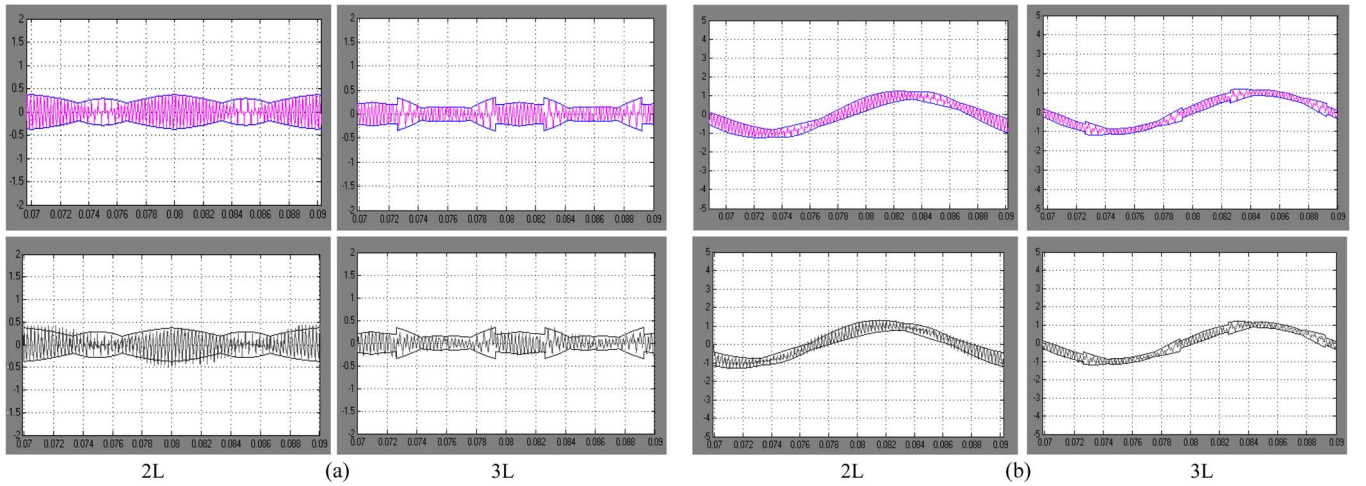


Fig. 8. Simulation (colored, top) and experimental (gray, bottom) results for 2L and 3L inverters, $m = 1/3$. (a) Current ripple with calculated peak-to-peak amplitude. (b) Instantaneous output current with calculated current envelopes.

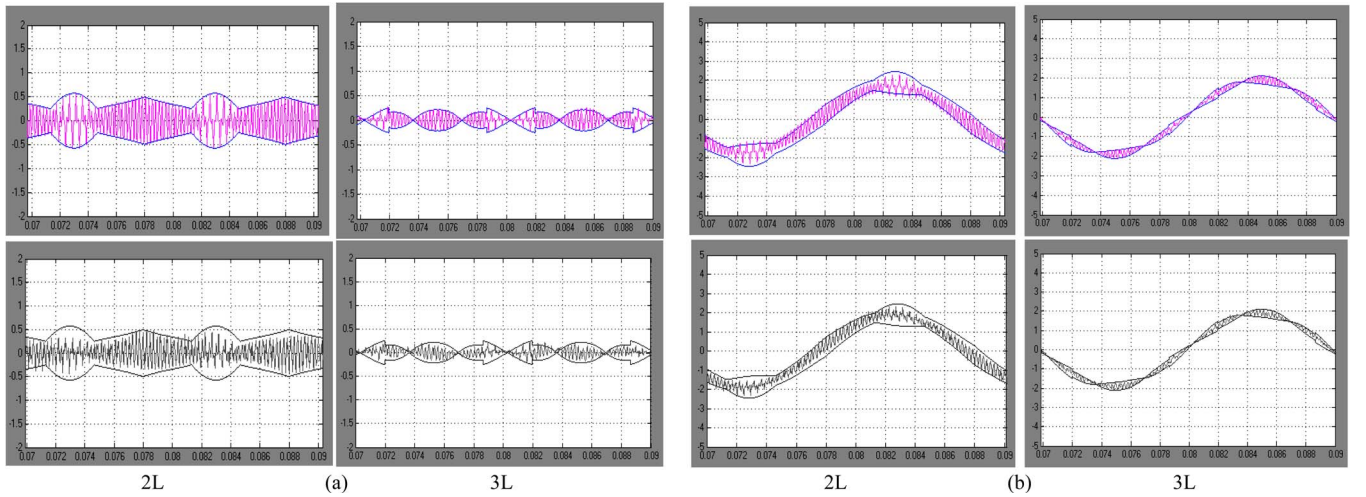


Fig. 9. Simulation (colored, top) and experimental (gray, bottom) results for 2L and 3L inverters, $m = 2/3$. (a) Current ripple with calculated peak-to-peak amplitude. (b) Instantaneous output current with calculated current envelopes.

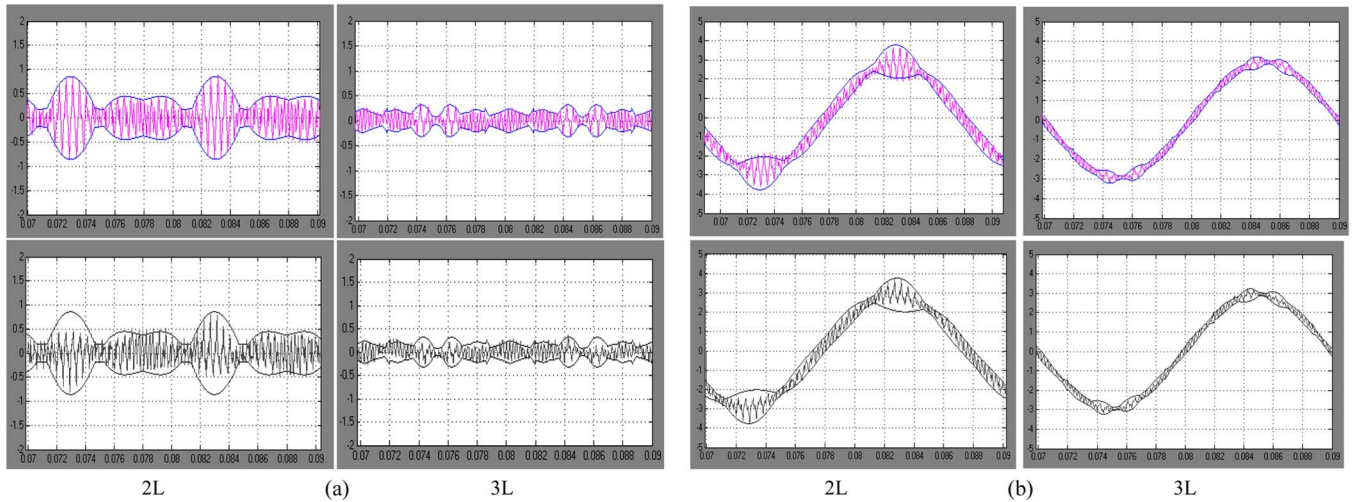


Fig. 10. Simulation (colored, top) and experimental (gray, bottom) results for 2L and 3L inverters, $m = 1$. (a) Current ripple with calculated peak-to-peak amplitude. (b) Instantaneous output current with calculated current envelopes.

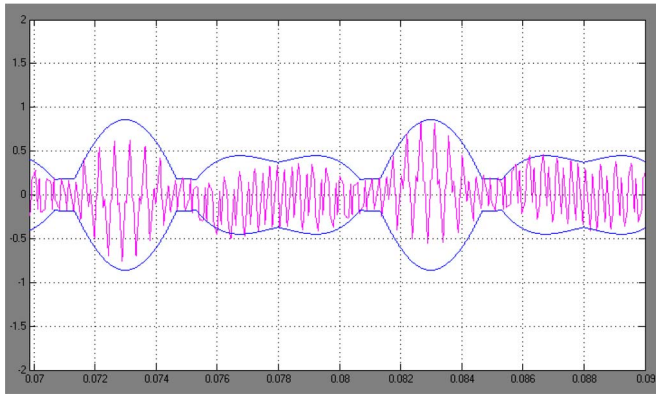


Fig. 11. Simulation results for the 2L inverter, $m = 1$, accounting for dead-time and considering a slightly higher load inductance (+15%) [see Fig. 10(a)].

(gray traces). Left and right diagrams are corresponding to 2L and 3L inverters with the same y -axis range for easier comparison. In Figs. 8(a)–10(a), the current ripple evaluated by (32) is depicted, whereas in Figs. 8(b)–10(b), the phase current is shown.

It can be noticed that simulation results perfectly match the calculated envelopes, for all the considered cases. Experimental results are also in good agreement with the analytical developments; just a slightly lower current ripple can be observed. This small mismatch is more emphasized in the 2L case, for high modulation indexes. It has been verified that the main origin of the observed lower value lies in the inverter dead-time, being not compensated in the experimental implementation but not considered in both simulations and analytical developments. Furthermore, the load (motor) inductance has been probably slightly underestimated. In order to prove these considerations, additional simulations have been carried out, introducing dead-time and slightly increasing the load inductance (+15%, ≈ 28 mH), showing a better matching with the experimental results. As an example, in Fig. 11, the case $m = 1$ for the 2L inverter is shown, corresponding to Fig. 10(a). It can be noticed that the effect of dead-time is to slightly reduce the current ripple, changing the envelope profile and causing an asymmetry of the positive and negative envelopes.

V. CONCLUSION

This paper has given the analysis and comparison of instantaneous output current ripple in three-phase 2L and 3L inverters. The peak-to-peak ripple evaluation in the 2L inverter is performed by analyzing the output voltage waveforms. It is shown that ripple evaluation in the 3L inverter can be carried out either as an extension of the analysis of the 2L inverter or by directly analyzing the 3L inverter output voltage waveform. The same procedure can be extended to the case of more than three levels.

Normalized peak-to-peak current ripple is introduced, and different ripple diagrams are given for 2L and 3L inverters, making possible a comparison considering the same output voltage range or the same dc voltage supply. In particular, reference is made to centered SVM for both 2L and 3L in-

verters. Readable and effective ripple maps are introduced to emphasize the ripple distribution in the fundamental period for the whole voltage modulation range of 2L and 3L inverters. As expected, the comparison shows that the ripple in the 3L inverter is generally lower than the ripple in the 2L inverter in case of the same output voltage range.

The analytical developments have been verified with numerical simulations and corresponding experimental tests for various modulation indexes, showing a good matching.

REFERENCES

- [1] D. Zhao, V. S. S. P. K. Hari, G. Narayanan, and R. Ayyanar, "Space-vector-based hybrid pulsewidth modulation techniques for reduced harmonic distortion and switching loss," *IEEE Trans. Power Electron.*, vol. 25, no. 3, pp. 760–774, Mar. 2010.
- [2] D. Holmes and T. A. Lipo, *Pulse Width Modulation for Power Converters—Principles and Practice*. Piscataway, NJ, USA: Wiley-IEEE Press, 2003, ser. IEEE Press Series on Power Engineering, pp. 215–257.
- [3] J. W. Kolar, H. Ertl, and F. C. Zach, "Minimizing the current harmonics RMS value of three-phase PWM converter systems by optimal and sub-optimal transition between continuous and discontinuous modulation," in *Proc. 22nd IEEE PESC*, Cambridge, MA, USA, Jun. 24–27, 1991, pp. 372–381.
- [4] D. Casadei, G. Serra, A. Tani, and L. Zarri, "Theoretical and experimental analysis for the RMS current ripple minimization in induction motor drives controlled by SVM technique," *IEEE Trans. Ind. Electron.*, vol. 51, no. 5, pp. 1056–1065, Oct. 2004.
- [5] X. Zhang and J. Spencer, "Study of multisampled multilevel inverters to improve control performance," *IEEE Trans. Power Electron.*, vol. 27, no. 11, pp. 4409–4416, Nov. 2012.
- [6] B. Vafakhah, J. Salmon, and A. M. Knight, "A new space-vector PWM with optimal switching selection for multilevel coupled inductor inverters," *IEEE Trans. Ind. Electron.*, vol. 57, no. 7, pp. 2354–2364, Jul. 2010.
- [7] M. M. Prats, J. M. Carrasco, and L. G. Franquelo, "Effective algorithm for multilevel converters with very low computational cost," *Electron. Lett.*, vol. 38, no. 22, pp. 1398–1400, Oct. 2002.
- [8] S. Wei, B. Wu, F. Li, and C. Liu, "A general space vector PWM control algorithm for multilevel inverters," in *Proc. 18th Annu. IEEE APEC Expo.*, Miami Beach, FL, USA, Feb. 9–13, 2003, pp. 562–568.
- [9] Y. H. Lee, D. H. Kim, and D. S. Hyun, "Carrier based SVPWM method for multi-level system with reduced HDF," in *Conf. Rec. IEEE IAS Annu. Meeting*, Rome, Italy, Oct. 8–12, 2000, pp. 1996–2003.
- [10] P. C. Loh, D. G. Holmes, Y. Fukuta, and T. A. Lipo, "Reduced common-mode modulation strategies for cascaded multilevel inverters," *IEEE Trans. Ind. Appl.*, vol. 39, no. 5, pp. 1386–1395, Sep./Oct. 2003.
- [11] B. P. McGrath, D. G. Holmes, and T. A. Lipo, "Optimized space vector switching sequences for multilevel inverters," *IEEE Trans. Power Electron.*, vol. 18, no. 6, pp. 1293–1301, Nov. 2003.
- [12] F. Wang, "Sine-triangle versus space-vector modulation for three-level PWM voltage-source inverters," *IEEE Trans. Ind. Appl.*, vol. 38, no. 2, pp. 500–506, Mar./Apr. 2002.
- [13] G. Grandi and J. Loncarski, "Simplified implementation of optimised carrier-based PWM in three-level inverters," *Electron. Lett.*, vol. 50, no. 8, pp. 631–633, Apr. 10, 2014.
- [14] S. Srinivas and K. Ramachandra Sekhar, "Theoretical and experimental analysis for current in a dual-inverter-fed open-end winding induction motor drive with reduced switching PWM," *IEEE Trans. Ind. Electron.*, vol. 60, no. 10, pp. 4318–4328, Oct. 2013.
- [15] A. Ruderman, "Understanding PWM current ripple in star-connected AC motor drive," *IEEE Power Electron. Soc. Newslett.*, vol. 21, no. 2, pp. 14–17, 2009, 2nd quarter.
- [16] D. Jiang and F. Wang, "Current-ripple prediction for three-phase PWM converters," *IEEE Trans. Ind. Appl.*, vol. 50, no. 1, pp. 531–538, Jan./Feb. 2014.
- [17] G. Grandi and J. Loncarski, "Evaluation of current ripple amplitude in three-phase PWM voltage source inverters," in *Proc. 8th Int. Conf. CPE*, Ljubljana, Slovenia, Jun. 5–7, 2013, pp. 156–161.
- [18] G. Grandi and J. Loncarski, "Evaluation of current ripple amplitude in five-phase PWM voltage source inverters," in *Proc. IEEE EUROCON*, Zagreb, Croatia, Jul. 1–4, 2013, pp. 1073–1080.

- [19] G. Grandi and J. Loncarski, "Analysis of peak-to-peak current ripple amplitude in seven-phase PWM voltage source inverters," *Energies*, vol. 6, no. 9, pp. 4429–4447, Aug. 2013.
- [20] G. Grandi, J. Loncarski, and C. Rossi, "Comparison of peak-to-peak current ripple amplitude in multiphase PWM voltage source inverters," in *Proc. 15th Conf. EPE Appl.*, Lille, France, Sep. 3–5, 2013, pp. 1–10.
- [21] D. Jiang and F. Wang, "A general current ripple prediction method for the multiphase voltage source converter," *IEEE Trans. Power Electron.*, vol. 29, no. 6, pp. 2643–2648, Jun. 2014.
- [22] G. Grandi, J. Loncarski, and R. Seebacher, "Effects of current ripple on dead-time analysis of three-phase inverters," in *Proc. IEEE ENERGY-CON*, Florence, Italy, Sep. 9–12, 2012, pp. 207–212.
- [23] C. N. M. Ho, V. S. P. Cheung, and H. S. H. Chung, "Constant-frequency hysteresis current control of grid-connected VSI without bandwidth control," *IEEE Trans. Power Electron.*, vol. 24, no. 11, pp. 2484–2495, Nov. 2009.
- [24] D. G. Holmes, R. Davoodnezhad, and B. P. McGrath, "An improved three-phase variable-band hysteresis current regulator," *IEEE Trans. Power Electron.*, vol. 28, no. 1, pp. 441–450, Jan. 2013.
- [25] A. Shukla, A. Ghosh, and A. Joshi, "Hysteresis modulation of multilevel inverters," *IEEE Trans. Power Electron.*, vol. 26, no. 5, pp. 1396–1409, May 2011.
- [26] D. Jiang and F. Wang, "Variable switching frequency PWM for three-phase converters based on current ripple prediction," *IEEE Trans. Power Electron.*, vol. 28, no. 11, pp. 4951–4961, Nov. 2013.
- [27] J. H. Seo, C. H. Choi, and D. S. Hyun, "A new simplified space-vector PWM method for three-level inverters," *IEEE Trans. Power Electron.*, vol. 16, no. 4, pp. 545–550, Jul. 2001.



Jelena Loncarski (S'11) received the Dipl.-Ing. and M.Sc. degrees from the Faculty of Electrical Engineering, University of Belgrade, Belgrade, Serbia, in 2007 and 2010, respectively, and the Ph.D. degree from the Department of Electrical Engineering, University of Bologna, Bologna, Italy, in 2014.

In April 2014, she joined the Department of Engineering Sciences, Ångström Laboratory, Uppsala University, Uppsala, Sweden, as a Postdoctoral Researcher. Her main research in-

terests are focused on power electronic circuits and power electronic converters for renewable energy sources.



Obrad Dordevic (S'11–M'13) received the Dipl.-Ing. degree in electronic engineering from the University of Belgrade, Belgrade, Serbia, in 2008. He received the Ph.D. degree from Liverpool John Moores University, Liverpool, U.K., in 2013.

He is currently a Lecturer with Liverpool John Moores University. His main research interests are in the areas of power electronics, electrostatic precipitators, and advanced variable-speed drives.



Gabriele Grandi (M'00–SM'13) received the M.Sc. (*cum laude*) and Ph.D. degrees in electrical engineering from the University of Bologna, Bologna, Italy, in 1990 and 1994, respectively.

He joined the Department of Electrical Engineering, University of Bologna, where he has been a Research Associate since 1995 and an Associate Professor since 2005. In 2013, he was qualified as a Full Professor of electrical engineering. He has published more than 120 papers in conference proceedings and inter-

national journals. His main research interests are focused on power electronic circuits and photovoltaics.